This is the accepted manuscript made available via CHORUS. The article has been published as:

Magic-angle magnonic nanocavity in a magnetic moiré superlattice

Jilei Chen, Lang Zeng, Hanchen Wang, Marco Madami, Gianluca Gubbiotti, Song Liu, Jianyu Zhang, Zifeng Wang, Wenhao Jiang, Yan Zhang, Dapeng Yu, Jean-Philippe Ansermet, and Haiming Yu

Phys. Rev. B **105**, 094445 — Published 31 March 2022

DOI: 10.1103/PhysRevB.105.094445

Magic-angle magnonic nanocavity in a magnetic Moiré superlattice

Jilei Chen,[1, 2, 3] Lang Zeng,[2] Hanchen Wang,[2] Marco Madami,[4] Gianluca Gubbiotti,[5] Song Liu,[1, 3] Jianyu Zhang,[2]
Zifeng Wang,[2] Wenhao Jiang,[6] Yan Zhang,[6] Dapeng Yu,[1, 3] Jean-Philippe Ansermet,[7, 1] and Haiming Yu[2, 1, 3, *]
[1]*Shenzhen Institute for Quantum Science and Engineering (SIQSE),*
Southern University of Science and Technology, Shenzhen, P. R. China
[2]*Fert Beijing Institute, MIIT Key Laboratory of Spintronics,*
School of Integrated Circuit Science and Engineering, Beihang University, Beijing 100191, China
[3]*International Quantum Academy (SIQA), and Shenzhen Branch,*
Hefei National Laboratory, Futian District, Shenzhen, P. R. China
[4]*Dipartimento di Fisica e Geologia, Università di Perugia, Perugia I-06123, Italy*
[5]*Istituto Ocina dei Materiali del Consiglio Nazionale delle Ricerche (IOM-CNR),*
c/o 5 Dipartimento di Fisica e Geologia, Perugia I-06123, Italy
[6]*School of Electronic and Information Engineering,*
Beihang University, Xueyuan Road 37, Beijing 100191, China
[7]*Institute of Physics, Ecole Polytechnique Fédérale de Lausanne (EPFL), 1015, Lausanne, Switzerland*

(Dated: March 9, 2022)

Moiré superlattices have recently been extensively studied in both electronic and photonic systems, e.g. magic-angle bilayer graphene showing superconductivity and twisted bilayer photonic crystals leading to magic-angle lasers. However, the Moiré physics is barely studied in the field of magnonics, i.e. in using spin waves for information processing. In this work, we report magnon flat band formation in twisted bilayer magnonic crystals at the optimal "magic angle" and interlayer exchange coupling combination using micromagnetic simulations. At the flat-band frequency, magnons undergo a strong two-dimensional confinement with a lateral scale of about 185 nm. The magic-angle magnonic nanocavity occurs at the AB stacking region of a Moiré unit cell, unlike its photonic counterpart which is at the AA region, due to the exchange-induced magnon spin torque. The magnon flat band originates from band structure reformation induced by interlayer magnon-magnon coupling. Our results enable efficient accumulation of magnon intensity in a confined region that is key for potential applicationssuch such as magnon Bose-Einstein condensation and even magnon lasing.

I. INTRODUCTION

Two layers of two-dimensional (2D) lattices placed on top of one another with a small twist angle can generate a new periodicity much larger than the original lattice constant, referred to as a "Moiré superlattice". Moiré superlattices of 2D materials, such as twisted bilayer graphene [1–9] are found to exhibit superconductivity [10] and correlated insulator states [11], and therefore have attracted tremendous interests in the emerging field of twistronics based on van der Waals layered materials. At the "magic angle" of approximately 1.1° of the Moiré superlattices, the Fermi velocity turns to zero and the energy band near the Fermi level becomes flat in twisted bilayer graphene leading to exotic electronics states. The concept of twistronics is also applied in photonics, where twisted bilayer photonic crystals [12–14] shows flat bands at small magic angles resulting in highly localized photonic modes with potential applications such as Bose-Einstein condensation. Magnons, the quanta of spin waves (SWs), being also bosons, are collective excitation of electron spins in magnetic materials and are intensively investigated in the perspective of magnonics or magnon spintronics [15–22], using magnons as information carriers in low-power-consumption spintronic devices [23, 24]. Magnonic crystals [25–30] are magnetic counterpart of photonic crystals. The magnon transport can be modulated by tuning the SW band gaps [31, 32] with novel functions such as reconfigurability [33–35] and nonreciprocity [36–39]. Recently, Gallardo et al. [40] has proposed to pattern arrays of heavy metal wires to impose periodical Dzyaloshinskii-Moriya interaction (DMI) on magnetic thin films. The simulations predict the emergence of flat bands in the bicomponent magnonic crystals with large DMI values. The heavy metal needed for the DMI [41] may severely affect the magnetic damping [42] and thus hinders its practical applications. Recent theoretical works report novel magnon behavior in twisted bilayer magnets in the presence of DMI [43, 44] and stacking domain walls [45]. However, magnons studied in these works are at extremely high frequencies (energy) making them difficult for practical applications in coherent magnonics operating typically at GHz frequencies [22]. Up to now, magnon flat bands and magnonic nanocavities in Moiré magnonic-crystal systems have not been reported.

In this Letter, we report magnon flat bands formed in magnetic Moiré superlattices by stacking two square antidot lattices with a finite twist angle (referred as "magic angle"). The results from micromagnetic simulations reveal that the perfect flat band emerges at an optimal combination of the "magic angle" and interlayer exchange coupling, and covers almost half of the first magnonic Brillouin zone (BZ) in the reciprocal space. Due to zero group velocity and high density of states of magnons at the flat band frequency, a highly localized SW mode i.e. magnonic nanocavity is discovered at the center of one Moiré unit cell with AB bilayer stacking. This is analogous to, but fundamentally different from, the recently discovered magic-angle photonic nanocavity [14] occurring always at the AA stacking region of Moiré photonic superlattices. The emergence of the magnon flat band is attributed to the lowest band formed by the mode anti-crossings in the SW dispersion due to interlayer magnon-magnon coupling [46–49]. The magic-angle magnonic nanocavity possesses a quality factor approximately two orders of magnitude higher than that of the non-flat-band mode, and exhibits a narrow spatial linewidth of about 185 nm inversely associated with the flat-band wavevector bandwidth.

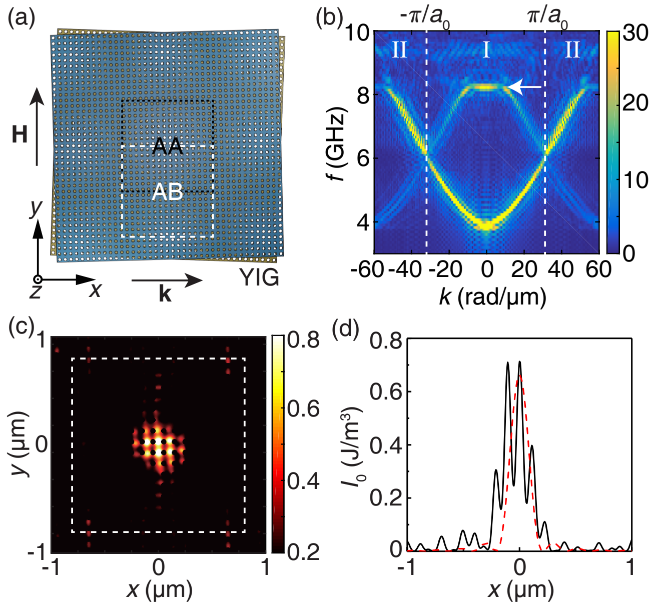

FIG. 1. (a) Schematic illustration of a YIG-based magnetic Moiré superlattice with a twist angle of $\theta = 3.5°$. The white dashed (black dotted) square represents the Moiré unit cell with AB (AA) stacking region at its center. A magnetic field of 50 mT is applied in the y direction. (b) SW dispersion obtained from micromagnetic simulations with the interlayer exchange coupling of $A_{12} = 11$ μJ/m^2. The white dashed lines represent the BZ boundaries, which define the first BZ ("I") and second BZ ("II"). (c) The spatial distribution of the magnetization dynamics (m_x in the bottom layer) at $t = 4.3$ ns with AB stacking after the start of continuous excitation. One Moiré unit cell is indicated by the white dashed square being the same white dashed region marked in (a). A magnonic nanocavity is formed at its center (AB stacking region). A line-cut of the magnon intensity at $y = 0$ is presented in (d), where the calculation by Eq. 3 (red dashed curve) yields a linewidth of 185 nm.

II. RESULTS AND DISCUSSION

The magnetic Moiré superlattice considered in this work is depicted in Fig. 1(a), which consists of two identical yttrium iron garnet (YIG) layers twisted by an angle θ. YIG thin films with low magnetic damping [50, 51] have recently been achieved and demonstrated experimentally for coherent magnonics. The saturation magnetization, intralayer exchange and magnetic damping are set as $M_{\mathrm{S}} = 140$ kA/m, $A_{11} = 3.7 \times 10^{-12}$ J/m and $\alpha = 0.0001$, respectively [52]. Each YIG layer is patterned into an antidot square lattice [13, 25] with a periodicity of $a_0 = 100$ nm and an antidot diameter of $d = 50$ nm, which can be fabricated with cutting-edge nanotechnology [20, 53]. The thickness of a single layer is set as 2 nm. Two layers are separated by 2 nm and coupled with the interlayer exchange A_{12}. By rotating one layer with respect to the other, a Moiré superlattice is then formed as shown in Fig. 1(a). The Moiré lattice constant can be estimated using $a_{\mathrm{m}} = a_0/\theta$ [12], where a_0 is the lattice constant of a single layer magnonic crystal being 100 nm. With $\theta = 3.5°$, the Moiré lattice constant is estimated to be approximately 1.6 μm. A Moiré unit cell is then a 1.6 μm × 1.6 μm region, e.g the black dotted square (with AA stacking region at the center) or the white dashed square (with AB stacking region at the center) in Fig. 1(a). In this work, we take the white region as the Moiré unit cell. The simulated structure covers an area of 6 μm × 6 μm in the xy plane with a cell size of 5 nm × 5 nm. A sinusoidal microwave pulse is applied in the middle of the investigated structure with a width of 20 nm in x direction for obtaining the full SW dispersion spectra, mimicking a nano-stripline in experiments [54]. The excited magnon wavevector then points along the x direction. A magnetic field of 50 mT is applied along the y axis, so the Damon-Eshbach SW configuration [55, 56] is investigated.

Figure 1(b) shows the SW dispersion from the micromagnetic simulation [61] performed at the center of the Moiré unit cell (white dashed square in Fig. 1(a)). Here, we set the twist angle $\theta = 3.5°$ and the interlayer exchange coupling $A_{12} = 11$ μJ/m^2, which is about two orders of magnitude weaker than the Ruderman-Kittel-Kasuya-Yosida exchange interaction in metallic spin valves [57, 58], one order of magnitude weaker than those at YIG/Co [46] and YIG/Py [59] interfaces and comparable with that in YIG/Au/YIG magnon valves [60]. The interlayer dipolar interaction is also included in the micromagnetic simulations based on OOMMF [61]. The excitation microwave power is set to be -10 dBm to maintain in the linear regime. The OOMMF is a finite difference micromagnetic solver. It was used to model the YIG based artificial Moiré superlattice which has dimensions much larger than the atomic scale. The two-dimensional Fourier transformation is performed on dynamic magnetization components in order to obtain the magnonic band structure. Compared with a single layer magnonic crystal (see Supplementary Material [62]), an unexpected flat band appears at around 8.2 GHz marked by the white arrow in Fig. 1(b). The magnonic flat band covers a broad wavevector range from -15 rad/μm to 15 rad/μm, that is about half of the first BZ of the magnonic crystal marked as "I" in Fig. 1(b) with BZ boundaries (white dashed lines) at ± 31.4 rad/μm corresponding to $\pm\pi/a_0$. The flat band locates around $k = 0$ (or Γ point) which is fundamentally different from its electronic [6] and photonic [14] counterparts as well as from the Moiré 2D magnets [43, 45], all of which exhibits a mini-flatband around the K point in the band structure. The flat band in the magnetic Moiré superlattice gives rise to zero magnon group velocity over a large wavevector range. As a result, a large number of magnons are "trapped" at the center of the Moiré unit cell to form a magnonic nanocavity as shown in the spatial map of magnon intensity (Fig. 1(c)) with excitation at the flat-band frequency (8.2 GHz), where the white dashed square represents the same region as that in Fig. 1(a). A single spectrum of the magnon intensity extracted along the center of the localized magnon mode is presented in Fig. 1(d), where the calculated magnon intensity by Eq. 3 (red dashed curve) yields a linewidth of 185 nm. The linewidth can be roughly considered as the diameter of the magnonic nanocavity formed in the magnetic Moiré superlattice. In addition to the strongly localized magnon mode, there appears also some weak propagating SWs, which could be resulted from the non-zero magnon group velocity at the border of the flat band. Notably, the magnonic nanocavity studied in this work is localized at the AB stacking region (see Fig. 1(a) and (c)), which is different to those in the magic-angle graphene superlattices [6] and twisted bilayer photononic crystals [12], where the effect always occurs at the AA stacking region. In the magnetic Moiré superlattice, it is observed that around the AA stacking region where the flat band disappears in the magnon dispersion and SWs are found to propagate away (see Supplementary Material [62]).

In the following, we investigate the formation of the Moiré flat band by tuning the twist angle θ and the interlayer exchange coupling A_{12}. At $\theta = 0$, the bilayer system is commensurate and its magnon dispersion resembles with that for single layer magnonic crystal as shown in Fig. 2(a). If there is no interlayer exchange ($A_{12} = 0$) but only magnetic dipolar interaction between two layers, flat bands also cannot be formed (see Supplementary Material [62]), although one may observe some "side bands" (e.g. indicated by white arrows in Fig. 2(c)) in superposition to the conventional magnonic crystal band structure. Therefore, the twist angle θ and the interlayer exchange coupling A_{12} are two key ingredients to create Moiré flat band in a bilayer magnonic crystal system. We first fix the interlayer exchange coupling at $A_{12} = 11$ μJ/m^2 and vary the twist angle θ. Figures 2(a)-(c) show three typical cases with different twist angles of $\theta = 0$, $\theta = 3°$ and $\theta = 6°$. In general, the magnonic flat band feature appears always around 8.2 GHz and survives within a relatively broad range of twist angles in stark contrast to electronic [6] and photononic [12] flat bands rely critically on the twist angle, i.e. the "magic angle". It is inferred that the frequency of flatband in magnonic Moiré superlattice is solely determined by the exchange coupling A_{12}. However, although the flat band sustains at different angles, the quality of the flatband or its flatness relies rather critically on the twist angle as shown in Fig. 2(d) with θ varying from 1.5° to 6°. The magnonic band flatness is characterized or defined as the linewidth of magnon density of state (DOS) around 8.2 GHz. The magnon DOS is calculated within the first BZ of the magnonic crystal and a Lorentz fitting is performed to obtain the Moiré flat-band bandwidth Δf_{m}, as shown in the inset of Fig. 2(d). The minimum of Δf_{m} peaks around 3.5°, which can be considered as the "magic angle" to form the Moiré magnonic flad band. By further increasing the twist angle, the side bands appear which reduce the flatness of the magnon band as shown in Fig. 2(d). In addition, by increasing the twisting angle, the magnonic band width decreases at the BZ boundaries, which is further discussed in Supplementary Material [62]. Then, by fixing the twist angle at 3.5°, we vary the interlayer exchange coupling A_{12}. With $A_{12} = 6$ μJ/m^2 (Fig. 2(e)), a curved magnon band appears around 6.8 GHz but the calculated Moiré bandwidth Δf_{m} is quite large, i.e. does not exhibit good flatness. With a larger interlayer exchange $A_{12} = 10$ μJ/m^2 (Fig. 2(f)), the curved magnon band becomes flat, and the frequency of the flat band rises to approximately 7.9 GHz. A mini-flatband at the ground state (3.7 GHz) is also observed whose wavevector range corresponds approximately to $2\pi/a_{\mathrm{m}}$. The Moiré flat band at 7.9 GHz is about 10 times broader covering more than half of the first magnonic BZ and re-appears in the second magnonic BZ (around ± 60 rad/μm). By further increasing the interlayer exchange to $A_{12} = 14$ μJ/m^2 (Fig. 2(g)), the Moiré flat band shifts up in frequency to about 8.8 GHz with a much smaller wavevector range and deteriorated flatness. Magnonic band structures at more values of A_{12} are presented in Supplementary Material [62], from which, the Moiré flat-band bandwidths are extrapolated and plotted in Fig. 2(h). The Moiré flat band sustains a high-quality flatness (with $\Delta f_{\mathrm{m}} < 0.2$ GHz) over a relatively large range of A_{12} from 8 μJ/m^2 to 12 μJ/m^2 (yellow shaded area in Fig. 2(h)). In general, we find the quality (flatness) of the Moiré flat band is determined by the combination of the twist angle θ and interlayer

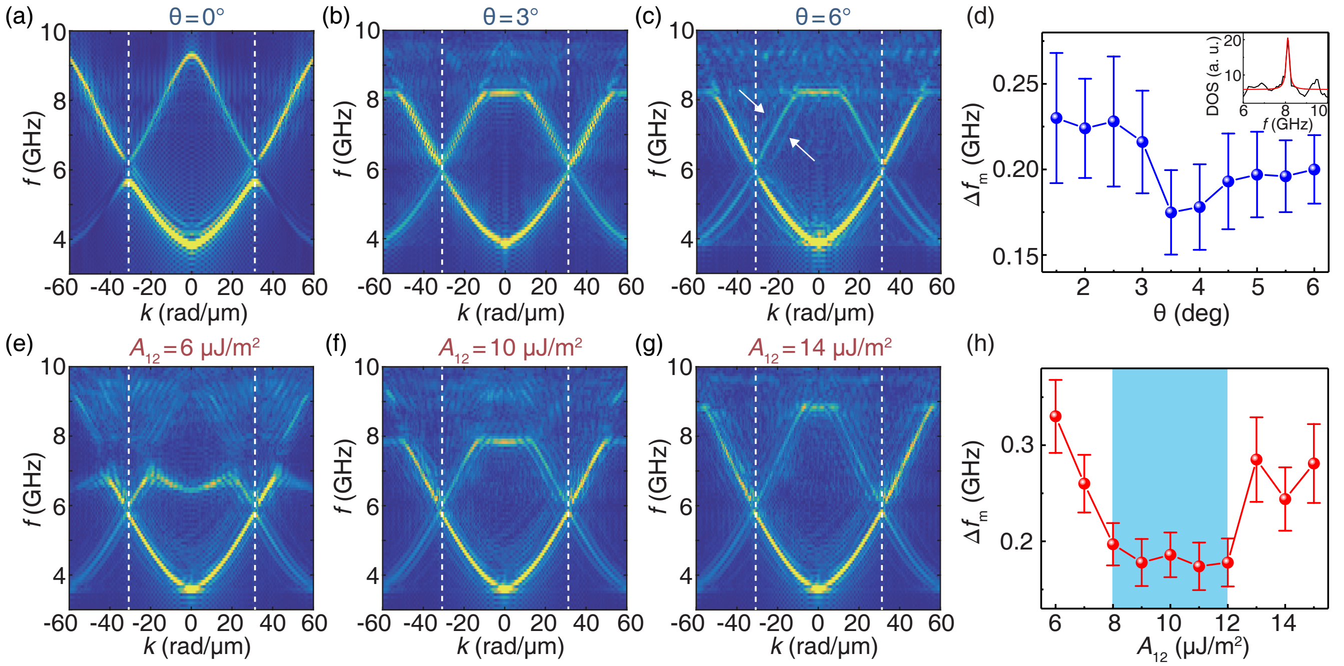

FIG. 2. (a) SW dispersion on commensurate bilayer magnonic crystal i.e. with $\theta = 0°$. (b) SW dispersion at the Moiré unit cell center (AB stacking region) with $\theta = 3°$. (c) SW dispersion at the Moiré unit cell center (AB stacking region) with $\theta = 6°$. White arrows indicate the side bands. The interlayer exchange coupling is fixed at $A_{12} = 11$ μJ/m^2 in (a)-(c). (d) Moiré flat-band bandwidth $\Delta f_{\rm m}$ as a function of twist angle θ. $\Delta f_{\rm m}$ is extrapolated from the linewidth of magnon density of states (DOS) around 8.2 GHz shown in the inset as an example at $\theta = 3.5°$. (e-g) Simulated SW dispersion at the Moiré unit cell center (AB stacking region) with a fixed twist angle $\theta = 3.5°$ and alternating interlayer exchange coupling of (e) 6 μJ/m^2, (f) 10 μJ/m^2 and (g) 14 μJ/m^2. (h) Interlayer exchange coupling dependence of Moiré flat-band bandwidth $\Delta f_{\rm m}$ with $\theta = 3.5°$. The light-blue shaded area highlights the region with high-quality Moiré flat band.

exchange coupling A_{12}. For instance, the combination of $\theta = 3.5°$ and $A_{12} = 11$ μJ/m^2 gives rise to an optimal Moiré flat band as shown in Fig. 1(b). In other word, the "magic angle" to form the Moiré flat band is closely associated with the interlayer exchange strength.

At an optimal combination of twist angle θ and interlayer exchange coupling A_{12}, a high-quality flat band is formed in the SW dispersion as shown in the inset of Fig. 3(a). We study and compare the flat-band mode (8.2 GHz, red arrow) and propagating mode (5 GHz, blue arrow) with a temporal excitation pulse as shown in Fig. 3(a) with 2 ns duration. The time-dependent magnetization dynamics $m_{\rm x}$ at the position of $x = 0$ is shown in Fig. 3(b) for excitation at 5 GHz and in Fig. 3(c) for excitation at 8.2 GHz (the flat-band frequency). In Fig. 3(b), the microwave pulse at 5 GHz is applied starting from 1 ns and instantly magnetization is found to oscillate with a reasonably large amplitude as shown in the blue curve. At the falling edge of the pulse (right edge of the yellow shaded area), the magnon spatial map (inset of Fig. 3(b)) reveals clear propagating SWs with a wavelength of approximately 300 nm that corresponds well with the wavevector at the blue arrow in the inset of Fig. 3(a). After the pulse is switched off, an abrupt decay of magnon intensity is observed in Fig. 3(b)). However, the remanent small amplitude can sustain over a much longer time scale. Such phenomenon can be described by the following equation

$$\mathcal{A}_{\rm sw} = C_1 \exp(-t/\tau_{\rm m}) + C_2 \exp(-t/\tau_0) \qquad (1)$$

where $\mathcal{A}_{\rm sw}$ represents the SW amplitude, C_1 and C_2 are two time-independent prefactors, $\tau_{\rm m}$ is the decay time for propagating magnon, and τ_0 is the decay time caused by the intrinsic damping of YIG, respectively. Due to lacking of localization for propagating SWs in Fig. 3(b)), $\tau_{\rm m}$ is found to be as small as 0.2 ns, yielding an effective cavity quality factor of $\mathcal{Q} = \omega\tau_{\rm m} = 6$, where ω is the angular frequency ($\omega = 2\pi f$). After 0.2 ns, the SW amplitude quickly relaxes to a more steady value and the frequency decreases to the FMR resonance 4 GHz. Then it would need much longer time to fully relax or damp to equilibrium magnetization state corresponding to the magnetic damping of YIG $\tau_0 = 1/\alpha\omega$. Taking the intrinsic damping of YIG to be 1×10^{-4} [50, 51], one attains $\tau_0 = 398$ ns. Now if the excitation is made at the flat-band frequency being 8.2 GHz, the SW intensity accumulates within the pulse duration (Fig. 3(c)) and quickly surpasses that of non-flatband mode (Fig. 3(b)). At the pulse falling edge (3 ns), the SW amplitude for the flat-band mode is more

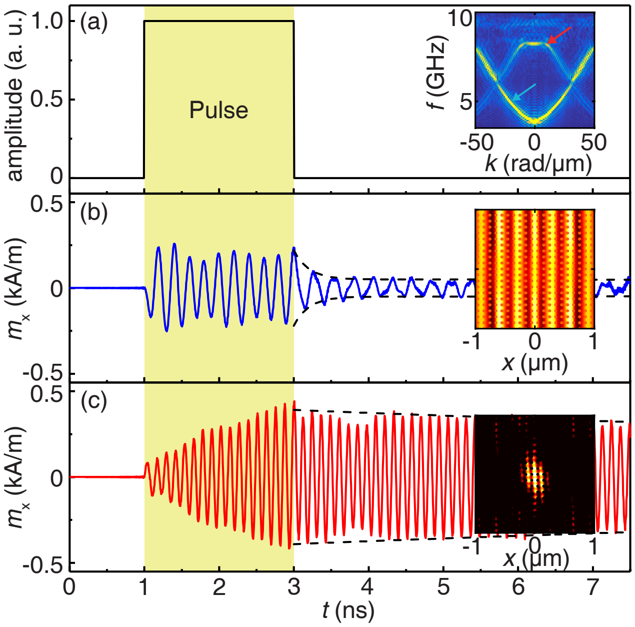

FIG. 3. (a) Microwave pulse applied in the bilayer magnetic Moiré superlattice with duration of 2 ns. The inset shows SW dispersion at $\theta = 3.5°$ and $A_{12} = 11\ \mu\text{J/m}^2$, where the red (blue) arrow indicates the flat-band mode at 8.2 GHz (a regular propagating mode at 5 GHz). (b) Time-domain magnetization dynamics m_x at 5 GHz in the center of a Moiré unit cell (AB stacking region). The inset presents the magnon spatial distribution at the falling edge of the pulse (3 ns), where clear SW propagation is observed. The black dashed line is an exponential fit to the decay after the pulse is switched off. (c) Temporal magnetization oscillation at the flat-band frequency (8.2 GHz). The yellow shaded area suggests the pulse duration. The magnon intensity is found to increase with time within the pulse duration reaching a maximum at the pulse falling edge (3 ns), where the magnon spatial distribution is presented in the inset forming a magnonic nanocavity around the AB stacking region. The black line is an exponential fit to the decay after the pulse is switched off.

than double of that for the non-flat-band mode. Moreover, a majority of the SW intensity is confined in a very small spacial region at the AB stacking area (inset of Fig. 3(c)). For the flatband mode at 8.2 GHz, the magnonic nanocavity is then formed due to the zero SW group velocity and a peak in magnon density state. By fitting the magnetization dynamics in Fig. 3(c) with Eq. 1, magnon relaxation time $\tau_\text{m} = 20$ ns is obtained, leading to an effective quality factor $\mathcal{Q} = \omega\tau_\text{m} = 1030$. This high quality factor of magnonic nanocavity is essential for the realization of highly localized magnon excitation for magnon Bose-Einstein condensation (BEC) [63–65] and even "magnon lasing" [66] in the future. The above described magic-angle magnonic nanocavity exhibits a distinctive feature: the confinement does not rely on a full forbidden band, but rather occurs at the flat band with a peak in magnon density of states. This confinement mechanism is fundamentally different from the nanocavity [67] or nanochannel [68] created by the defects within a conventional magnonic crystal, where the magnon confinement relies essentially on a full magnonic band gap. Given that, there is no allowed states in the magnonic band gap, magnonic crystals act as a mirror (or a wall) to confine the defect magnon states. Contrary to Fig. 3(b), after the pulse is switched off, the magnon frequency maintains at 8.2 GHz not decreasing to 4 GHz. This intriguing feature implies that the localized magnons in the twisted bilayer mutually couple to form a self-oscillating hybridized mode at 8.2 GHz.

In Fig. 4, we further investigate the relation between magnonic nanocavity and the formation of the magnon flat band in magnetic Moiré superlattices with different twist angles. First of all, we find that to trigger the strong magnon confinement does not require high excitation power, so we lower the rf power from -10 dBm (Fig. 1) to -30 dBm (Fig. 4) in order to fully avoid the nonlinear spin precession in the system. The conversion between the microwave excitation field and the power is studied by the high frequency structure simulator (see Supplementary Material [62]). Magnetic Moiré superlattices with twist angles of $\theta = 1°$, $3.5°$ and $6°$ are depicted in Fig. 4(a), (b) and (c) showing different Moiré lattice constant of 5.73 μm, 1.64 μm and 0.95 μm, respectively. The corresponding calculated magnon "flat-band" dispersion at these three angles are shown in Fig. 4(d), (e) and (f). In general, the results of these three twist angles all exhibit a flat-band feature in the magnon dispersion, although with different "quality" or "flatness". The emergence of magnon flat band over a relatively large range of twist angle offers much easier implementation of magic-angle magnonic device in general applications than its counterpart in electronics, e.g. magic-angle bilayer graphene, which demands critically a small angle of a typical 1.1° [6]. The excitation at the magnon flat band increases the magnon DOS dramatically and creates strong magnon confinement at the center of a Moiré unit cell (AB stacking region) as shown in Fig. 4(h) with a magic angle $\theta = 3.5°$. If the twist angle deviates from the optimal one (or magic angle), the flat band becomes not so "flat". With a small twist angle of 1°, the flat band is rounded up and shows a small "bump" around $k = 0$ (Fig. 4(d)), which eventually results in a poor magnon confinement at the Moiré unit cell center as shown in Fig. 4(g). With a large twist angle of 6°, the magnon flat band appears to be disruptive, which projects into the real space as some "leakage" between two neighbouring magnonic nanocavities. Therefore, for $A = 11\ \mu\text{J/m}^2$, the magnonic nanocavity with the optimal quality occurs at or around the "magic angle" of 3.5°.

Finally, we investigate the formation mechanism of the magnon flat bands and discuss the origin of the magic

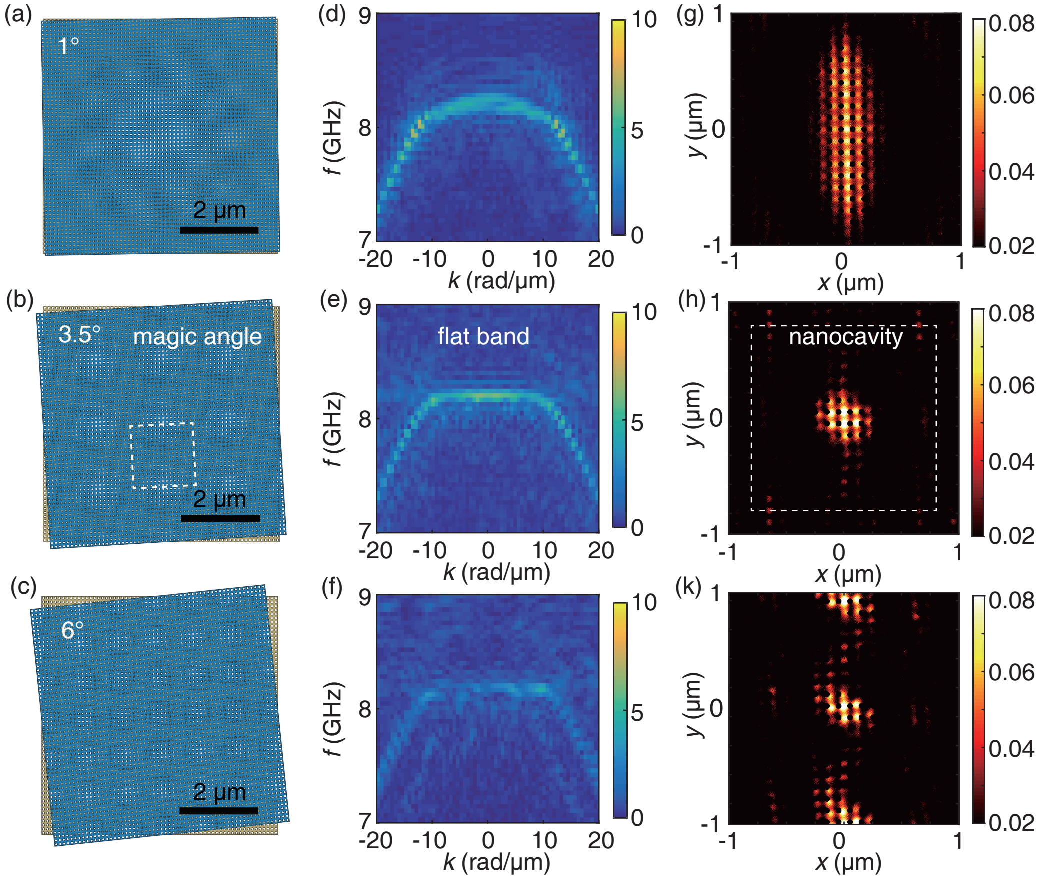

FIG. 4. (a)-(c) Schematic illustrations of twisted bilayer magnonic crystals with twist angles of (a) 1°, (b) 3.5° and (c) 6°, respectively. The interlayer exchange coupling is fixed at 11 μJ/m^2 The white dashed square indicates a Moiré unit cell with an area of 1.64 μm×1.64 μm. (d)-(f) The SW dispersion near the flat-band region simulated at the center of the Moiré unit cell for magnetic Moiré superlattices with different twist angles of (d) 1°, (e) 3.5° and (f) 6°. The excitation microwave power is set to be -30 dBm, smaller than that in Fig. 1. (g)-(k) Magnetization m_x snapshots of a 2 μm×2 μm area at $t = 4.3$ ns after the start of continuous microwave excitation with twist angles of (g) 1°, (h) 3.5° and (k) 6°.

angle in magnetic Moiré superlattices. We start with one single layer of magnonic crystal with square antidot lattices. Conventional magnonic band gaps are observed at magnonic BZ boundaries (see Supplementary Material [62]), very similar to those shown in Fig. 2(a) for zero-twist-angle bilayer system. By twisting one single magnonic crystal layer with respect to the same SW wavevector k, we find the magnonic band shifts in both directions in the twisted layer (see Supplementary Material [62]), analogous to the side bands indicated by the white arrows in Fig. 2(c). If there is no interlayer exchange coupling (only interlayer dipolar interaction), three individual magnonic branches can be observed in the magnon dispersion without significant mode hybridization as illustrated in Fig. 5(a). The interlayer exchange coupling stimulates the strong interlayer magnon-magnon coupling [46–48], which manifests as the anti-crossing between different magnonic branches, comparable to those observed in cavity magnonics [69] between magnons and cavity photons [70–73]. Therefore, the interlayer exchange coupling generates multiple anti-crossings at the meeting points between three individual magnonic branches (one from untwisted layer and two from the twisted layer), which eventually evolves to four quasi-flatband, two from the upper band (C1 and C2) and two from the lower band (V1 and V2), as shown in Fig. 5(b). Microscopically, the effective interlayer exchange interaction considering its integration in the whole Moir superlattice is crucially dependent on the interlayer stacking configurations and preserves Moiré translational symmetry as $A_{12}(r) = A_{12}(r + R)$, where r is the position within the Moiré supercell, and R is a Moiré superlattice vector. The origin of flat bands in magic-angle twisted bilayer graphene are different from the magnonic flat bands. The flatness in magic-angle twisted bilayer graphene have a topological origin with nonvanishing Chern numbers and are reminiscent of pseudo Landau levels [74, 75], which emerge from the coupling between Dirac fermions of graphene with the pseudo magnetic fields generated by the spatial

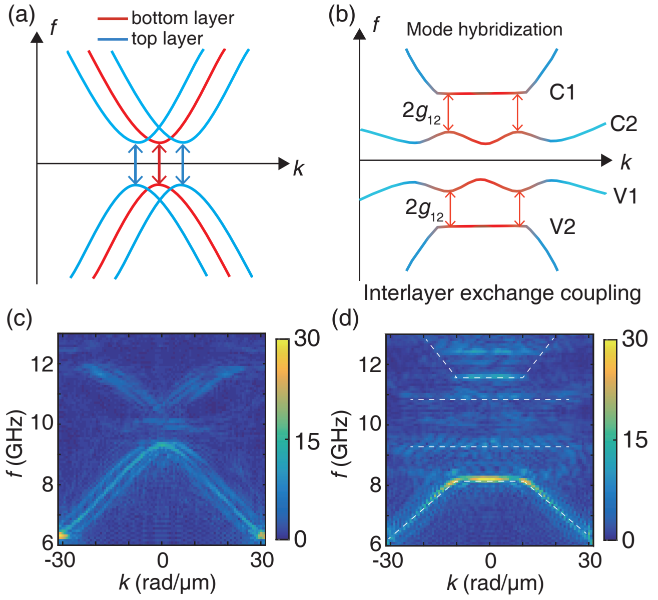

FIG. 5. (a) Sketch of uncoupled magnetic Moiré superlattice with shifted bands in the wavevector space. The red (blue) curve indicates the magnonic bands of the bottom (top) layer magnonic crystal. The bottom layer is aligned with the antenna, whereas the top layer is rotated with respect to the bottom layer as shown in Fig. 4. The arrows mark the band gap of the magnonic crystals. (b) With strong interlayer exchange coupling, the magnon branches start to hybridize and form several flat bands due to the mode anticrossings. Four quasi-flatbands are labelled as C1, C2, V1 and V2. Red arrows indicate the new gaps induced by the mode hybridization, that is about twice the magnon-magnon coupling strength g_{12}. (c) A zoom-in simulated magnonic band structure near the band gap in the absence of the interlayer exchange coupling. (d) Simulation results on magnonic band structure near the band gap with $A_{12} = 11$ μJ/m^2. The twist angle is fixed at $\theta = 3.5°$. Four quasi-flat bands are marked by white dashed lines.

varying interlayer hopping term. For the magic-angle magnonic nanocavity studied in this work, the flat bands observed in Fig. 5(b) and Fig. 2 originate from the lowest quasi-flat band V2 [74] as shown in Fig. 5. Prior to the mode hybridization, the magnonic crystals provide large magnon band gaps, and consequently after mode hybridization the quasi-flat bands C2 and V1 are still far apart in frequency and cannot be unified to one flat mode. Nevertheless, all four quasi-flat bands can be vaguely observed in the Fig. 5(d) with the lowest mode V2 being the strongest, which is essentially the flat band we discuss in this work. Thus, one key element to form the flat bands apart from the magic angle is the interlayer exchange coupling. The role of the interlayer exchange coupling in magnonic magic-angle system is comparable to the interlayer separation in its photonic [12] counterparts. The interlayer magnon-magnon coupling strength (g_{12}) manifests itself as the anti-crossing gap ($2g_{12}$) between the magnon branches of the upper and lower layers and is given rise by the interlayer-exchange-induced [46–48] magnon spin torque [76–79] τ_{12}^{m}, that is proportional to the effective interlayer exchange field $\mathbf{h}_{\mathrm{eff}} = A_{12}|\nabla_z \mathbf{m}|^2$. Then we obtain

$$g_{12} \propto \tau_{12}^{\mathrm{m}} = \mathbf{m} \times A_{12} \frac{\partial^2 \mathbf{m}}{\partial z^2}. \tag{2}$$

Eq. 2 suggests that the magnetization gradient in the z direction is required to generate a strong interlayer magnon-magnon coupling in order to form the magnon flat bands. At the edge of the Moiré lattice, namely the AA region, the magnonic crystal lattices of two layers are overlapped (see Supplementary Material for magnetic texture distributions [62]), and thus the magnetic texture gradient is minimized, which results in a weak interlayer magnon-magnon coupling [46]. At the center of the Moiré lattice (the AB region), however, the magnetic texture difference between the two layers is maximized, and thus the interlayer exchange becomes most effective to provide strong magnon-magnon coupling similar to the case of exchange springs [46, 80], and can eventually generate flat bands as shown in Fig. 5. This explains why the magnonic nanocavities occur always at the AB region different from the photonic nanocavities [14] at the AA region due to the nature of the exchange interaction. In this work, we focus on the low-frequency flat bands which are due to the magnon-magnon mode hybridization. It is shown that for magnon-photon hybridization, the topological Chern number of the coupled wave becomes quantized into nonzero integers [81]. The effect of topology on the magnonic flat bands in magnetic Moiré superlattice required further investigatigation.

The flat band provides a high magnon DOS, i.e. a wide range of wavevector distribution Δk_0 at a given magnon frequency. In analog to the magic-angle photonic nanocavities [14], such high DOS is a key to generate the highly confined mode. The spatial distribution of the magnon intensity $I_0(x)$ for the magic-angle magnonic nanocavity induced by the magnon flat band can be calculated by the summation or superposition of all SW modes (or states) at the one-and-the-same flat-band frequency ω_0. After taking approximation of continuous k variation (see Supplementary Material [62]) in magnon dispersion, one derives

$$I_0(x) = \frac{A^2 S}{\pi^2} \left| \frac{\sin\left(\frac{1}{2}\Delta k_0 x\right)}{x} \right|^2, \tag{3}$$

where A is the SW amplitude assumed to be constant for all modes at the flat band. S stands for the area of one Moiré unit cell. By taking the flat-band wavevector bandwidth $\Delta k_0 \approx 30$ rad/μm extracted from results in Fig. 1(b), one can calculate the magnon intensity distribution $I_0(x)$ based on Eq. 3 with a spatial linewidth $\Delta x_0 = 185$ nm, which is comparable with the intensity distribution attained from simulation results in Fig. 1(d).

III. CONCLUSIONS AND OUTLOOK

To conclude, we have investigated the Moiré magnetic superlattices with a twist angle using micromagnetic simulations. The results show the emergence of magnon flat bands in the magnon dispersion, which eventually results in a magnonic nanocavity with a diameter of about 185 nm. The flatness of the flatband and also the quality of the magnonic nanocavity is found to be highly tunable with two major physical quantities, i.e. the twist angle θ and the interlayer exchange A_{12}. The ideal flat band is achieved with the combination of the "magic angle" $\theta = 3.5^\circ$ and interlayer exchange $A_{12} = 11\ \mu\mathrm{J/m}^2$ with reasonably good tolerance with the deviation from the optimal values. The results on the pulse simulation demonstrate that the magic-angle magnonic nanocavity with a high quality factor enables a strong enhancement or accumulation of magnon intensity inside the nanocavity, which provides great perspectives to achieve magnon BEC in the Moiré magnetic superlattices and to pave the way towards "magnon lasing" with high intensities. The magnonic flat band observed in this work is found to be easily tunable with an applied magnetic field as shown in the Supplementary Material [62], which enables the excitation of magic-angle magnonic nanocavity at different demanded frequencies. This field-tunablity of flat bands may be obvious for the magic-angle magnetic systems, but non-trivial for its electronic and photonic counterparts.

Finally, the formation of the magnon flat band is attributed to the mode anti-crossings in the magnon dispersion induced by interlayer magnon-magnon coupling. To generate experimentally the magnon flat band and realize the magic-angle magnonic nanocavity based on this artificial crystal with a periodicity on a 100 nm scale, we showed that we could adopt the simplified nanolithography technique as used in Moiré photonic nanocavity [14] where the effective exchange coupling is fixed and the twist angle is the only tuning parameter. By introducing a non-magnetic spacer between two magnonic-cyrstal stacks, one can tune the interlayer exchange by the thickness of the spacer with high sensitivity ruled by the RKKY interaction [82]. Recent demonstration on tunable magnon-magnon coupling [83] in synthetic antiferromagnets may also provide an experimental appoach to control the coupling strength. The nature of the interlayer exchange coupling explains the magnon confinement at the AB stacking region of the Moiré magnetic superlattices, which is fundamentally different from the magic-angle photonic nanocavity always at the AA region. The theoretical calculation indicates that broader flat band may introduce a even more focused magnoninc nanocavity, to be studied and achieved in experiments in the future. Last but not the least, our studies also contribute to the emerging field of three-dimensional (3D) magnonics [84, 85], where magnon propagation properties are modulated by the vertical interlayer coupling [86, 87] enabling the transition from 2D to 3D magnonic architectures.

ACKNOWLEDGMENTS

The authors acknowledge support from the NSF China under Grants 12074026, 12104208 and U1801661, the 111 Talent Program B16001, the National Key Research and Development Program of China Grants 2016YFA0300802 and 2017YFA0206200.

---

* haiming.yu@buaa.edu.cn

[1] E. Suárez Morell, J. D. Correa, P. Vargas, M. Pacheco, and Z. Barticevic, Flat bands in slightly twisted bilayer graphene: Tight-binding calculations. Phys. Rev. B **82**, 121407(R) (2010).

[2] R. Bistritzer, and A. H. MacDonald, Unconventional superconductivity in magic-angle graphene superlattices. Proc. Natl. Acad. Sci. U.S.A. **108**, 12233 (2011).

[3] Q. Tong, H. Yu, Q. Zhu, Y. Wang, X. Xu, and W. Yao, Topological mosaics in moir superlattices of van der Waals heterobilayers. Nat. Phys. **13**, 356-362 (2017).

[4] K. Kim, A. DaSilva, S. Huang, B. Fallahazad, S. Larentis, T. Taniguchi, K. Watanabe, B. J. LeRoy, A. H. MacDonald, and E. Tutuc, Tunable moiré bands and strong correlations in small-twist-angle bilayer graphene. Proc. Natl. Acad. Sci. U.S.A. 114, **114**, 3364 (2017).

[5] Y. Cao, V. Fatemi, A. Demir, S. Fang, S. L. Tomarken, J. Y. Luo, J. D. Sanchez-Yamagishi, K. Watanabe, T. Taniguchi, E. Kaxiras, R. C. Ashoori, and P. Jarillo-Herrero, Correlated insulator behaviour at half-filling in magic-angle graphene superlattices. Nature **556**, 80-84 (2018).

[6] Y. Cao, V. Fatemi, S. Fang, K. Watanabe, T. Taniguchi, E. Kaxiras, and P. Jarillo-Herrero, Unconventional superconductivity in magic-angle graphene superlattices. Nature **556**, 43-50 (2018).

[7] X. Lu, P. Stepanov, W. Yang, M. Xie, M. A. Aamir, I. Das, C. Urgell, K. Watanabe, T. Taniguchi, G. Zhang, A. Bachtold, A. H. MacDonald and D. K. Efetov, Superconductors, orbital magnets and correlated states in magic-angle bilayer graphene. Nature **574**, 20-23 (2019).

[8] F. Wu, A. H. MacDonald, and I. Martin, Theory of phonon-mediated superconductivity in twisted bilayer graphene. Phys. Rev. Lett. **121**, 257001 (2018).

[9] T. J. Peltonen, R. Ojajärvi, and T. T. Heikkilä, Theory of phonon-mediated superconductivity in twisted bilayer graphene. Phys. Rev. B **98**, 220504(R) (2018).

[10] M. Yankowitz, S. Chen, H. Polshyn, Y. Zhang, K. Watanabe, T. Taniguchi, D. Graf, A. F. Young, and C. R. Dean, Tuning superconductivity in twisted bilayer graphene. Science **1064**, 1059-1064 (2019).

[11] X. Zhang, K.-T. Tsai, Z. Zhu, W. Ren, Y. Luo, S. Carr, M. Luskin, E. Kaxiras, and K. Wang, Correlated insulating states and transport signature of superconductivity in

twisted trilayer graphene superlattices. Phys. Rev. Lett. **127**, 166802 (2021).

[12] K. Dong, T. Zhang, J. Li, Q. Wang, F. Yang, Y. Rho, D. Wang, C. P. Grigoropoulos, J. Wu, and J. Yao, Flat bands in magic-angle bilayer photononic crystals at small twists. Phys. Rev. Lett. **126**, 223601 (2021).

[13] B. Lou, N. Zhao, M. Minkov, C. Guo, M. Orenstein, and S. Fan, Theory for Twisted Bilayer photononic Crystal Slabs. Phys. Rev. Lett. **126**, 136101 (2021).

[14] X.-R. Mao, Z.-K. Shao, H.-Y. Luan, S.-L. Wang, and R.-M. Ma, Magic-angle lasers in nanostructured moiré superlattice. Nat. Nanotechnol. **16**, 1099-1105 (2021).

[15] V. Vlaminck, and M. Bailleul, Current-induced spin-wave Doppler shift. Science **322**, 410 (2008).

[16] Y. Kajiwara, K. Harii, S. Takahashi, J. Ohe, K. Uchida, M. Mizuguchi, H. Umezawa, H. Kawai, K. Ando, K. Takanashi, S. Maekawa, and E. Saitoh, Transmission of electrical signals by spin-wave interconversion in a magnetic insulator. Nature **464**, 262-266 (2010).

[17] V. V. Kruglyak, S. O. Demokrotiv, and D. Grundler, Magnonics. J. Phys. D: Appl. Phys. **43**, 264001 (2010).

[18] A. V. Chumak, V. I. Vasyuchka, A. A. Serga, and B. Hillebrands, Magnon spintronics. Nat. Phys. **11**, 453-461 (2015).

[19] L. J. Cornelissen, J. Liu, R. A. Duine, J. B. Youssef, and B. J. vanWees, Long-distance transport of magnon spin information in a magnetic insulator at room temperature. Nat. Phys. **11**, 1022-1026 (2015).

[20] A. Haldar, D. Kumar, and A. O. Adeyeye, A reconfigurable waveguide for energy-efficient transmission and local manipulation of information in a nanomagnetic device. Nat. Nanotechnol. **11**, 437-443 (2016).

[21] H. Yu, J. Xiao, and H. Schultheiss, Magnetic texture based magnonics. Phys. Rep. **905**, 1-59 (2021).

[22] P. Pirro, V. I. Vasyuchka, A. A. Serga and B. Hillebrands, Advances in coherent magnonics. Nat. Rev. Mater. (2021), https://doi.org/10.1038/s41578-021-00332-w.

[23] A. Khitun, M. Bao, and K. L. Wang, Magnonic logic circuits. J. Phys. D: Appl. Phys. **43**, 264005 (2010).

[24] G. Csaba, A. Papp, and W. Porod, Perspectives of using spin waves for computing and signal processing. Phys. Lett. A **11**, 948-953 (2016).

[25] S. Neusser, G. Durr, H. G. Bauer, S. Tacchi, M. Madami, G. Woltersdorf, G. Gubbiotti, C. H. Back, and D. Grundler, Anisotropic propagation and damping of spin waves in a nanopatterned antidot lattice. Phys. Rev. Lett. **105**, 067208 (2010).

[26] J. Ding, M. Kostylev, and A. O. Adeyeye, Magnonic crystal as a medium with tunable disorder on a periodical lattice. Phys. Rev. Lett. **107**, 047205 (2011).

[27] G. Gubbiotti, S. Tacchi, M. Madami, G. Carlotti, S. Jain, A. O. Adeyeye, and M. P. Kostylev, Collective spin waves in a bicomponent two-dimensional magnonic crystal. Appl. Phys. Lett. **100**, 162407 (2012).

[28] M. Krawczyk, and D. Grundler, Review and prospects of magnonic crystals and devices with reprogrammable band structure. J. Phys. Condens. Matter **26**, 123202 (2014).

[29] S. Tacchi, G. Gubbiotti, M. Madami, and G. Carlotti, Brillouin light scattering studies of 2D magnonic crystals. J. Phys. Condens. Matt. **29**, 073001 (2017).

[30] S. A. Díaz, T. Hirosawa, J. Klinovaja, and D. Loss, Chiral magnonic edge states in ferromagnetic skyrmion crystals controlled by magnetic fields. Phys. Rev. Res. **2**, 013231 (2020).

[31] S. Tacchi, F. Montoncello, M. Madami, G. Gubbiotti, G. Carlotti, L. Giovannini, R. Zivieri, F. Nizzoli, S. Jain, A. O. Adeyeye, and N. Singh, Band diagram of spin waves in a two-dimensional magnonic crystal. Phys. Rev. Lett. **107**, 127204 (2011).

[32] S. Tacchi, G. Duerr, J. W. Klos, M. Madami, S. Neusser, G. Gubbiotti, G. Carlotti, M. Krawczyk, and D. Grundler, Forbidden band gaps in the spin-wave spectrum of a two-dimensional bicomponent magnonic crystal. Phys. Rev. Lett. **109**, 137202 (2012).

[33] J. Topp, D. Heitmann, M. P. Kostylev, and D. Grundler, Making a reconfigurable artificial crystal by ordering bistable magnetic nanowires. Phys. Rev. Lett. **104**, 207205 (2010).

[34] Q. Wang, A. V. Chumak, L. Jin, H. Zhang, B. Hillebrands, and Z. Zhong, Making a reconfigurable artificial crystal by ordering bistable magnetic nanowires. Phys. Rev. B **95**, 134433 (2017).

[35] A. K. Mondal, C. Banerjee, A. Adhikari, A. K. Chaurasiya, S. Choudhury, J. Sinha, S. Barman, and A. Barman, Spin-texture driven reconfigurable magnonics in chains of connected Ni80Fe20 submicron dots. Phys. Rev. B **101**, 224426 (2020).

[36] M. Mruczkiewicz, M. Krawczyk, G. Gubbiotti, S. Tacchi, Y. A. Filimonov, D. V. Kalyabin, I. V. Lisenkov, and S. A. Nikitov, Nonreciprocity of spin waves in metallized magnonic crystal. New J. Phys. **15**, 113023 (2013).

[37] O. Gladii, M. Haidar, Y. Henry, M. Kostylev, and M. Bailleul, Frequency nonreciprocity of surface spin wave in permalloy thin films. Phys. Rev. B **93**, 054430 (2016).

[38] J. Chen, T. Yu, C. Liu, T. Liu, M. Madami, K. Shen, J. Zhang, S. Tu, M. S. Alam, K. Xia, M. Wu, G. Gubbiotti, Y. M. Blanter, G. E. W. Bauer, and H. Yu, Excitation of unidirectional exchange spin waves by a nanoscale magnetic grating. Phys. Rev. B **100**, 104427 (2019).

[39] J. Chen, H. Yu, and G. Gubbiotti, Unidirectional spin-wave propagation and devices. J. Phys. D: Appl. Phys. **55**, 123001 (2022).

[40] R. A. Gallardo, D. Cortés-Ortuño, T. Schneider, A. Roldán-Molina, F. Ma, R. E. Troncoso, K. Lenz, H. Fangohr, J. Lindner, and P. Landeros, Flat bands, indirect gaps, and unconventional spin-wave behavior induced by a periodic Dzyaloshinskii-Moriya interaction. Phys. Rev. Lett. **122**, 067204 (2019).

[41] X. Ma, G. Yu, C. Tang, X. Li, C. He, J. Shi, K. L. Wang, and X. Li, Interfacial Dzyaloshinskii-Moriya interaction: effect of 5d band filling and correlation with spin mixing conductance. Phys. Rev. Lett. **120**, 157204 (2018).

[42] Y. Sun, H. Chang, M. Kabatek, Y. Y. Song, Z. Wang, M. Jantz, W. Schneider, M. Wu, E. Montoya, B. Kardasz, B. Heinrich, S. G. E. te Velthuis, H. Schultheiss, and A. Hoffmann, Damping in yttrium iron garnet nanoscale films capped by platinum. Phys. Rev. Lett. **111**, 106601 (2013).

[43] Y.-H. Li, and R. Cheng, Moiré magnons in twisted bilayer magnets with collinear order. Phys. Rev. B **102**, 094404 (2020).

[44] D. Ghader Magnon magic angles and tunable Hall conductivity in 2D twisted ferromagnetic bilayers. Sci. Rep. **10**, 15069 (2020).

[45] C. Wang, Y. Gao, H. Lv, X. Xu, and D. Xiao, Stacking domain wall magnons in twisted van der Waals magnets. Phys. Rev. Lett. **125**, 247201 (2020).

[46] S. Klingler, V. Amin, S. Geprägs, K. Ganzhorn, H. Maier-Flaig, M. Althammer, H. Huebl, R. Gross, R. D. McMichael, M. D. Stiles, S. T. B. Goennenwein, and M. Weiler, Spin-torque excitation of perpendicular standing spin waves. Phys. Rev. Lett. **120**, 127201 (2018).

[47] J. Chen, C. Liu, T. Liu, Y. Xiao, K. Xia, G. E. W. Bauer, M. Wu, and H. Yu, Strong interlayer magnon-magnon coupling in magnetic metal-insulator hybrid nanostructures. Phys. Rev. Lett. **120**, 217202 (2018).

[48] H. Qin, S. J. Hämäläinen, and S. van Dijken, Exchange-torque-induced excitation of perpendicular standing spin waves in nanometer-thick YIG films. Sci. Rep. **8**, 5755 (2018).

[49] Y. Li, W. Cao, V. P. Amin, Z. Zhang, J. Gibbons, J. Sklenar, J. Pearson, P. M. Haney, M. D. Stiles, W. E. Bailey, V. Novosad, A. Hoffmann, and W. Zhang,, Coherent spin pumping in a strongly coupled magnon-magnon hybrid system. Phys. Rev. Lett. **124**, 117202 (2020).

[50] H. Chang, P. Li, W. Zhang, T. Liu, A. Hoffmann, L. Deng, and M. Wu, Nanometer-thick yttrium iron garnet films with extremely low damping. IEEE Magn. Lett. **5**, 6700 (2014).

[51] H. Yu, O. Allivy Kelly, V. Cros, R. Bernard, P. Bortolotti, A. Anane, F. Brandl, R. Huber, I. Stasinopoulos, and D. Grundler, Magnetic thin-film insulator with ultra-low spin wave damping for coherent nanomagnonics. Sci. Rep. **4**, 6848 (2014).

[52] M. Wu, A. Hoffmann, R. E. Camley, and R.L. Stamps, Solid State Physics: Recent advances in magnetic insulators from spintronics to microwave applications, 64 Academic Press (2013).

[53] S. Watanabe, V. S. Bhat, K. Baumgaertl, and D. Grundler, Direct observation of worm-like nanochannels and emergent magnon motifs in artificial ferromagnetic quasicrystals. Adv. Funct. Mater. **30**, 2001388 (2020).

[54] F. Ciubotaru, T. Devolder, M. Manfrini, C. Adelmann, and I. P. Radu, All electrical propagating spin wave spectroscopy with broadband wavevector capability. Appl. Phys. Lett. **109**, 012403 (2016).

[55] J. R. Eshbach, and R. W. Damon, Surface Magnetostatic Modes and Surface Spin Waves. Phys. Rev. **118**, 1208 (1960).

[56] K. Yamamoto, G. C. Thiang, P. Pirro, K.-W. Kim, K. Everschor-Sitte, and E. Saitoh, Topological characterization of classical waves: The topological origin of magnetostatic surface spin waves. Phys. Rev. Lett. **122**, 217201 (2019).

[57] A. Fert Nobel Lecture: Origin, development, and future of spintronics. Rev. Mod. Phys. **80**, 1517 (2008).

[58] S. O. Demokritov, C. Bayer, S. Poppe, M. Rickart, J. Fassbender, B. Hillebrands, D. I. Kholin, N. M. Kreines, and O. M. Liedke, Control of interlayer exchange coupling in Fe/Cr/Fe trilayers by ion beam irradiation. Phys. Rev. Lett. **90**, 097201 (2003).

[59] Y. Fan, P. Quarterman, J. Finley, J. Han, P. Zhang, J. T. Hou, M. D. Stiles, A. J. Grutter, and L. Liu, Manipulation of coupling and magnon transport in magnetic metal-insulator hybrid structures. Phys. Rev. Appl. **13**, 061002(R) (2020).

[60] H. Wu, L. Huang, C. Fang, B. S. Yang, C. H. Wan, G. Q. Yu, J. F. Feng, H. X. Wei, and X. F. Han, Magnon valve effect between two magnetic insulators. Phys. Rev. Lett. **120**, 097205 (2018).

[61] M. Donahue, and D. Porter, OOMMF Users Guide, Version 1.0, National Institute of Standards and Technology, Gaithersburg, MD, interagency report nistir 6376 Edition (Sept 1999). URL http://math.nist.gov/oommf.

[62] See Supplemental Material for magnonic band structures of single layer magnonic crystals and uncoupled magnetic Moiré superlattices, magnonic band structure of the AA stacking region, magnonic band structures at more values of A_{12}, Power dependence of the magnonic nanocavity induced by flat bands, high frequency structure simulator of the excitation antenna, magnetization texture distributions at different regions in the Moiré superlattice, magnon intensity for the magic-angle magnonic nanocavity, tuning flat-band frequency by external magnetic fields.

[63] S. O. Demokritov, V. E. Demidov, O. Dzyapko, G. A. Melkov, A. A. Serga, B. Hillebrands, and A. N. Slavin, BoseEinstein condensation of quasi-equilibrium magnons at room temperature under pumping. Nature **443**, 430-433 (2006).

[64] T. Giamarchi, C. Rüegg, and O. Tchernyshyov, BoseEinstein condensation in magnetic insulators. Nat. Phys. **4**, 198-204 (2008).

[65] M. Schneider, T. Brächer, D. Breitbach, V. Lauer, P. Pirro, D. A. Bozhko, H. Yu. Musiienko-Shmarova, Björn Heinz, Q. Wang, T. Meyer, *et al.*, BoseEinstein condensation of quasiparticles by rapid cooling. Nat. Nanotechnol. **15**, 457-461 (2020).

[66] L. Berger, Multilayers as spin-wave emitting diodes. J. Appl. Phys. **81**, 4880 (1997).

[67] N. Kumar, and A. Prabhakar, Resonant spin wave excitations in a magnonic crystal cavity. J. Magn. Magn. Mater. **450**, 46-50 (2018).

[68] T. Schwarze, and D. Grundler, Magnonic crystal wave guide with large spin wave propagation velocity in CoFeB. Appl. Phys. Lett. **102**, 222412 (2013).

[69] B. Z. Rameshti, S. V. Kusminskiy, J. A. Haigh, K. Usami, D. Lachance-Quirion, Y. Nakamura, C.-M. Hu, H. X. Tang, G. E. W. Bauer, and Y. M. Blanter, Cavity magnonics. https://arxiv.org/abs/2106.09312.

[70] H. Huebl, C. W. Zollitsch, J. Lotze, F. Hocke, M. Greifenstein, A. Marx, R. Gross, and S. T. B. Goennenwein, High cooperativity in coupled microwave resonator ferrimagnetic insulator hybrids. Phys. Rev. Lett. **111**, 127003 (2013).

[71] X. Zhang, C.-L. Zou, L. Jiang, and H. X. Tang, Strongly Coupled Magnons and Cavity Microwave Photons. Phys. Rev. Lett. **113**, 156401 (2014).

[72] L. Bai, M. Harder, Y. P. Chen, X. Fan, J. Q. Xiao, and C.-M. Hu, Spin pumping in electrodynamically coupled magnon-photon systems. Sci. Rep. **114**, 227201 (2015).

[73] Y. Cao, P. Yan, H. Huebl, S. T. B. Goennenwein, and G. E. W. Bauer, Exchange magnon-polaritons in microwave cavities. Phys. Rev. B **91**, 094423 (2015).

[74] G. Tarnopolsky, A. J. Kruchkov, and A. Vishwanath, Origin of magic angles in twisted bilayer graphene. Phys. Rev. Lett. **122**, 106405 (2019).

[75] J. Liu, J. Liu, and X. Dai, Pseudo Landau level representation of twisted bilayer graphene: Band topology and implications on the correlated insulating phase. Phys. Rev. B **99**, 155415 (2019).

[76] J. C. Slonczewski, Initiation of spin-transfer torque by thermal transport from magnons. Phys. Rev. B **82**, 054403 (2010).

[77] P. Yan, X. S. Wang, and X. R. Wang, All-magnonic spin-transfer torque and domain wall propagation. Phys. Rev. Lett. **107**, 177207 (2011).

[78] J. Han, P. Zhang, J. T. Hou, S. A. Siddiqui, and L. Liu, Mutual control of coherent spin waves and magnetic domain walls in a magnonic device. Science **366**, 1121-1125 (2019).

[79] Y. Wang, D. Zhu, Y. Yang, K. Lee, R. Mishra, G. Go, S.-H. Oh, K. Cai, E. Liu, S. D. Pollard, *et al.*, Magnetization switching by magnon-mediated spin torque through an antiferromagnetic insulator. Science **366**, 1125-1128 (2019).

[80] K. L. Livesey, D. C. Crew, and R. L. Stamps, Spin wave valve in an exchange spring bilayer. Phys. Rev. B **73**, 184432 (2006).

[81] A. Okamoto, R. Shindou, and S. Murakami, Berry curvature for coupled waves of magnons and electromagnetic waves. Phys. Rev. B **102**, 064419 (2020).

[82] S. S. P. Parkin, R. Bhadra, and K. P. Roche, Oscillatory magnetic exchange coupling through thin copper layers. Phys. Rev. Lett. **66**, 2152-2155 (1991).

[83] Y. Shiota, T. Taniguchi, M. Ishibashi, T. Moriyama, and T. Ono, Tunable magnon-magnon coupling mediated by dynamic dipolar interaction in synthetic antiferromagnets. Phys. Rev. Lett. **125**, 017203 (2020).

[84] G. Gubbiotti, T. Taniguchi, M. Ishibashi, T. Moriyama, and T. Ono, *Three-dimensional magnonics.* (Jenny Stanford, Singapore, 2019).

[85] A. Barman, G. Gubbiotti, S. Ladak, A. O. Adeyeye, M. Krawczyk, J. Gräfe, C. Adelmann, S. Cotofana, A. Naeemi, V. I. Vasyuchka, *et al.*, The 2021 magnonics Roadmap. J. Phys.: Condens. Matter **33**, 413001 (2021).

[86] G. Gubbiotti, X. Zhou, Z. Haghshenasfard, M. G. Cottam, and A. O. Adeyeye, Reprogrammable magnonic band structure of layered Permalloy/Cu/Permalloy nanowires. Phys. Rev. B **97**, 134428 (2018).

[87] P. Graczyk, M. Krawczyk, S. Dhuey, W.-G. Yang, H. Schmidt, and G. Gubbiotti, Magnonic band gap and mode hybridization in continuous permalloy films induced by vertical dynamic coupling with an array of permalloy ellipses. Phys. Rev. B **98**, 174420 (2018).